ARTICLE   OPEN

Check for updates

Third-order topological insulators with wallpaper fermions in Tl_4PbTe_3 and Tl_4SnTe_3

Ning Mao[1], Hao Wang[1], Ying Dai[1 ✉], Baibiao Huang[1] and Chengwang Niu [1 ✉]

Nonsymmorphic symmetries open up horizons of exotic topological boundary states and even generalize the bulk–boundary correspondence, which, however, the third-order topological insulator in electronic materials are still unknown. Here, by means of the symmetry analysis and k · p models, we uncover the emergence of long-awaited third-order topological insulators and the wallpaper fermions in space group I4/mcm (No.140). Based on this, we present the hourglass fermion, fourfold-degenerate Dirac fermion, and Möbius fermion in the (001) surface of Tl_4XTe_3 ($X = $ Pb/Sn) with a nonsymmorphic wallpaper group $p4g$. Remarkably, 16 helical corner states reside on eight corners in Kramers pair, rendering the real electronic material of third-order topological insulators. More importantly, a time-reversal polarized octupole polarization is defined to uncover the nontrivial third-order topology, as is implemented by the 2nd and 3rd order Wilson loop calculations. Our results could considerably broaden the range of wallpaper fermions and lay the foundation for future experimental investigations of third-order topological insulators.

INTRODUCTION

Much of the recent interest has been prompted by the symmetry-protected topological quantum states, and in particular, the classification of topological electronic states is greatly enriched while including the crystalline symmetries[1–7]. A notable example is the topological crystalline insulator (TCI) protected by the symmorphic mirror or rotation symmetry, where twofold-degenerate surface fermions appear on particular surfaces preserving the corresponding symmorphic symmetry[8–11]. Only recently, this topological classification has started to reach out to the nonsymmorphic symmetries, combinations of point group operations and fractional translations, such as the hourglass fermion experimentally observed in KHgX family ($X = $ As, Sb, Bi)[12,13], and the Möbius insulators[14,15]. Moreover, a fourfold-degenerate Dirac fermion emerges, in contrast to the twofold degeneracy of conventional TCIs and time-reversal symmetry ($\mathbb{T}$) protected topological insulators (TIs)[16–18], on the surface of a topological insulating phase with multiple glide lines, representing an exception to fermion-doubling theorems[19]. Physically, the degeneracy and compatibility relation of surface states can be constrained to the irreducible co-representation of 17 two-dimensional (2D) wallpaper groups[19], and the hourglass fermion, Möbius insulators, and fourfold-degenerate Dirac fermion have been well studied in the all four nonsymmorphic wallpaper groups, pg, pmg, pgg and $p4g$[14,15,19–25].

On the other hand, the crystalline symmetries open up a horizon of topological bulk–boundary correspondence, extended with quantized quadrupole or octupole moments, revealing the presence of higher-order topological insulators (HOTIs)[26–29]. For which, the d-dimensional n^{th}-order ($n \geq 2$) topological phase holds gapless state at (d-n)-dimensional boundary but gapped state otherwise. Therefore the topology of HOTIs is localized at hinges and/or corners with chiral or helical modes, which is distinguished by the nested Wilson loop, i.e., 2nd and 3rd order ones for second-order TIs (SOTIs) and third-order TIs (TOTIs), respectively[26,30–35]. Despite being actively explored, efforts have mainly focused on the SOTIs[36–52], which have been observed experimentally in both

the metamaterials such as microwave[37], electrical circuit[39], and acoustics[41,46–48], and the electronic materials such as Bi[38] and Bi_4Br_4[52]. The TOTIs have only been limited to metamaterials, explicit electronic materials that enable the exploration of exotic quantum phenomena, including fractional corner charges[53–55] and filling anomaly[56], have so far been missing[26,34,46,57,58].

Here, we demonstrate the realization of wallpaper fermions and TOTIs in thallium compounds, Tl_4XTe_3 ($X = $ Pb/Sn), which have been overlooked as trivial insulators for years[59–62]. Correlated with two perpendicular glide mirrors in nonsymmorphic wallpaper groups, wallpaper fermions including hourglass fermion, fourfold-degenerate Dirac fermion, and Möbius fermion emerge in the surface spectrum. However, unlike nontrivial wallpaper fermions in the previous reports[7,12,13,19,20], the generalized $\mathbb{Z}_4$ invariant is trivial in our materials, which remarkably renders a gapped Wilson loop and allows us to implement the nested Wilson loop for the TOTIs nature. Indeed, the evaluated 3rd order Wilson loop for Tl_4XTe_3 is nonzero, confirming their nontrivial topology as the first family of TOTIs in electronic materials. Further analysis uncover that Tl_4XTe_3 are helical TOTIs with 16 nontrivial corner states residing on eight corners, very different from the reported chiral ones in metamaterials. Our results not only enrich the boundary of fundamental understanding for wallpaper fermion but also provide a route towards the realization of TOTIs.

RESULTS

Wallpaper fermions in nonsymmorphic wallpaper group

It is well known that the band degeneracies are closely related to the symmetries in 17 2D space groups, i.e., wallpaper groups[19,20]. The wallpaper group G can be thought of as a semi-direct product $G = T_{tp} \wedge Q$, where T_{tp} is a pure translation group of Bravis lattice composed of infinite group elements and Q is a factor group used to distinguish the symmorphic and nonsymmorphic wallpaper groups. For a symmorphic wallpaper group, Q is a pure point group composed of only the symmorphic symmetry operations, while the elements of Q can be replaced by screw-axis rotations

[1]School of Physics, State Key Laboratory of Crystal Materials, Shandong University, Jinan, China. ✉email: daiy60@sdu.edu.cn; c.niu@sdu.edu.cn
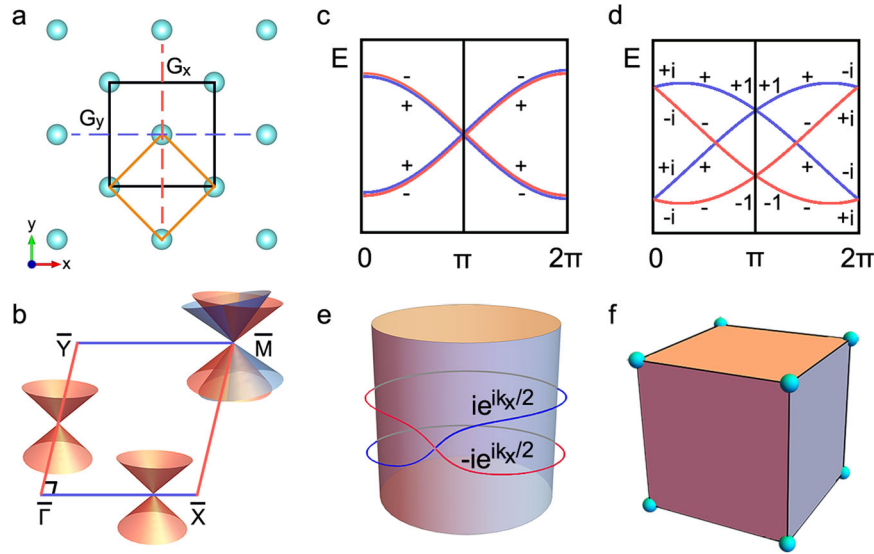
Fig. 1 Schematic demonstration for the wallpaper fermions and third-order topology. a Schematic of wallpaper group $p4g$ with two perpendicular glide lines $\mathbb{G}_{x/y}$ indicated with red/blue dashed lines. **b** Two categories of band crossings induced by $\mathbb{G}_{x/y}$ along the invariant paths, which are constrained by the commutation relations of $\mathbb{G}_{x/y}$ and $\mathbb{T}\mathbb{G}_{y/x}$. **c** When $\mathbb{G}_{x/y}$ anticommuting with $\mathbb{T}\mathbb{G}_{y/x}$, a fourfold-degenerate Dirac point appears at the zone boundary $k = \pi$, i.e., at M as in **b**. **d** When $\mathbb{G}_{x/y}$ commute with $\mathbb{T}\mathbb{G}_{y/x}$, the band crossing is twofold degenerate and an hourglass-shaped dispersion with an internal partner switching for each quadruplet appears. **e** Due to the $\mathbb{G}_{x/y}$ eigenvalues $g_{\pm x/y} = \pm ie^{-ik_{y/x}/2}$, surface states cannot go to the origin after a period of 2π, but a periodicity of 4π, featuring a Möbius fermion character. **f** Schematic of a helical third-order topological insulator with time-reversal polarized octupole moments.

and/or glide lines for a nonsymmorphic wallpaper group. Among the 17 wallpaper groups, there are 4 nonsymmorphic wallpaper groups and 13 symmorphic wallpaper groups, where only pgg and $p4g$ consist of one pair of perpendicular glide lines. Taking the nonsymmorphic wallpaper group $p4g$ as an example, we give a detailed description of the perpendicular glide lines. $p4g$ is given by a semi-direct product of the translation group T_{tp} and factor group Q', namely $p4g = T_{tp} \wedge Q'$. Indeed, factor group Q' is isomorphic to the point group $4mm$, while the perpendicular mirror lines in $4mm$ are replaced by the perpendicular glide lines, as illustrated in Fig. 1a. In addition, T_{tp} consists of elements $\{E|n_1\mathbf{t}_1 + n_2\mathbf{t}_2 + n_3(\mathbf{t}_1 + \mathbf{t}_2)/2\}$, where n_i ($i = 1, 2, 3$) are integers, $\mathbf{t}_1$, $\mathbf{t}_2$ represent the lattice translation along x and y directions, respectively, and $(\mathbf{t}_1 + \mathbf{t}_2)/2$ is the center translation that indicates a half-lattice translation when n_3 is odd.

In crystal momentum space, the symmetry $\{\mathbb{D}|t\}$ can only protect degeneracies in the invariant lines/points of the Brillouin Zone that satisfy $\mathbb{D}k \rightarrow k$. In this invariant space, the Hamiltonian of system commutes with $\{\mathbb{D}|t\}$ and can be block diagonalized into two sectors with two opposite eigenvalues. For $\mathbb{G}_{x/y}$, the invariant lines are $(\overline{\Gamma Y}, \overline{XM})/(\overline{\Gamma X}, \overline{YM})$, indicated with red/blue lines in Fig. 1b. Along the invariant lines, glide lines satisfy $\mathbb{G}_{x/y}^2 = -e^{-ik_{y/x}}$, so that one can get the eigenvalues as $g_{\pm x} = \pm ie^{-ik_y/2}$ and $g_{\pm y} = \pm ie^{-ik_x/2}$, which are ± 1 at $\overline{X}$, $\overline{Y}$, $\overline{M}$ and $\pm i$ at $\overline{\Gamma}$. Besides, $\mathbb{T}$ imposes further constraints to the above four momenta, which satisfy $\mathbb{T}^2 = -1$, guaranteeing the Kramers degeneracy. The Kramers pairs at $\overline{X}$, $\overline{Y}$, and $\overline{M}$ have the same eigenvalues, while that at $\overline{\Gamma}$ have the opposite eigenvalues. Apart from unitary symmetry, it has to mention that $(\overline{\Gamma Y}, \overline{XM})/(\overline{\Gamma X}, \overline{YM})$ are $\mathbb{T}\mathbb{G}_y/\mathbb{T}\mathbb{G}_x$ invariant lines that may induce a higher degeneracy.

Along the above four glide invariant lines, the connectivities of bands are constrained by the commutation relations of $\mathbb{G}_{x/y}$ and $\mathbb{T}\mathbb{G}_{y/x}$, which can be classified into two categories. Figure 1c shows the first category with anticommutation relation $\{\mathbb{G}_{x/y}, \mathbb{T}\mathbb{G}_{y/x}\} = 0$, the bands with opposite eigenvalues form a Kramers pair along the glide invariant lines. Moreover, at $k=\pi$, $\mathbb{G}_x$ and $\mathbb{G}_y$ anticommute with each other, i.e., $\{\mathbb{G}_x, \mathbb{G}_y\} = 0$, and

satisfy $\mathbb{G}_x^2 = \mathbb{G}_y^2 = +1$, a four-dimensional irreducible representations (Irreps) shows up, which results in the fourfold-degenerate Dirac fermion at the $\overline{M}$ point. This can be further seen by examining the $k \cdot p$ Hamiltonian around the momenta $\overline{M}$,

$$H_M = \tau_x(v_x\sigma_x k_x + v_y\sigma_y k_y). \tag{1}$$

At $\overline{M}$, the symmetry matrix can be written as $\mathbb{T} = i\sigma_y K$, $\mathbb{G}_x = \tau_y\sigma_x$, and $\mathbb{G}_y = \tau_y\sigma_y$, where τ and σ are Pauli matrices describing the sublattice and spin degrees of freedom. Clearly, the Dirac point remains intact for any glide lines allowed term, while for a $\mathbb{T}$-symmetric term $V_m = m\tau_z$, it introduces a gap and turns the system into either a TI or a trivial insulator.

The second category shown in Fig. 1d exhibits a hourglass-shaped dispersion with the commutation relation $[\mathbb{G}_{x/y}, \mathbb{T}\mathbb{G}_{y/x}] = 0$ along the momenta lines of $\overline{\Gamma Y}$ and $\overline{\Gamma X}$. The bands labeled with $g_{+x/y}$ and $g_{-x/y}$ belong to different Irreps and will cross each other over the $\overline{\Gamma Y}$ and $\overline{\Gamma X}$, leading to a symmetry-protected accidental degeneracy, as shown in Fig. 1b. Due to any hybridization between different Irreps is not allowed by the glide line, $k \cdot p$ Hamiltonian around the crossing point can take the block diagonal forms as

$$H(\mathbf{k}) = v_x k_x \sigma_x + v_y k_y \sigma_y, \tag{2}$$

where $\mathbf{k}$ represents the momenta of crossing point. Any $\mathbb{G}_{x/y}$ allowed terms cannot break the degeneracy, but only shift the position of the degenerate point along the glide line, leading to a presence of $\mathbb{G}_{x/y}$-protected twofold-degenerate Dirac fermion. Remarkably, the phase of $\mathbb{G}_{y/x}$ entrust the birth of Möbius fermion as illustrated in Fig. 1e. That means, when one go round the $k_{x/y}$ direction about a period, $k_x \rightarrow k_x + 2\pi$, the eigenstates switch places, and we need go around 4π to return to the origin.

Having demonstrated the possibility of symmetry-allowed band degeneracies in $p4g$, we aim now at showing that their topology, and remarkably, a third-order TI is obtained. In the presence of $\mathbb{T}$, zero-dimensional corner states originate from the time-reversal polarized octupole moment, which is quantized to 0 or 1/2 by the crystallographic symmetries. As presented in Supplementary Note,
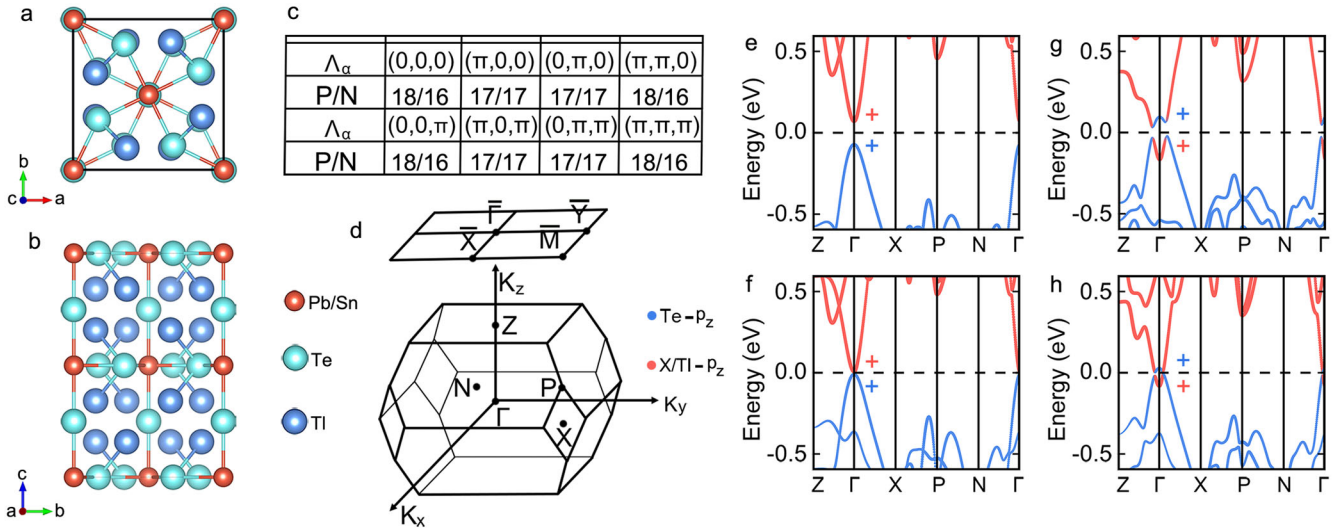
Fig. 2 Material candidates of wallpaper fermion and third-order topological insulators. a Top and **b** side views of Tl_4XTe_3 (X = Pb/Sn) conventional unit cell. **c** Numbers of occupied bands with positive (P) and negative (N) parities at eight $\mathbb{T}$-invariant momenta (Λ_α) with SOC. **d** Brillouin zone for the primitive unit cell of Tl_4XTe_3, and projected 2D (001) Brillouin zone. **e–h** Bulk band structures of e, g, Tl_4PbTe_3 and f, h, Tl_4SnTe_3 e, f, without and **g**, **h** with SOC. The bands are orbitally weighted with the contribution of Te-p_z and X/Tl-p_z states. The Fermi level is indicated with a dashed line.

together with inversion symmetry ($\mathbb{I}$), mirror and/or glide symmetries along three cartesian directions have to participate. Among the 2 nonsymmorphic wallpaper groups (p4g and pgg) that host fourfold-degenerate Dirac fermion, only *p4g* reside in all of the necessary symmetries to get the quantized time-reversal polarized octupole moment.

Material candidates

For the realization of the material, we focus on the ternary thallium compounds Tl_4XTe_3(X = Pb/Sn), which are known to be advanced thermoelectric and optoelectronic materials[63,64]. They crystallize in the tetragonal structure with a space group of I4/mcm as shown in Fig. 2a and b[65]. There are 32 atoms in a conventional cell, with 16 Tl atoms located at Wyckoff position 16*l*, 4 *X* atoms located at Wyckoff position 4*c*, and 12 Te atoms located at two Wyckoff positions 4*a* and 8*h*[66], respectively. The optimized lattice constants are a = 8.98/8.93 Å and c = 13.43/13.35 Å for Tl_4XTe_3 with X = Pb/Sn, almost the same as with the experimental values[63]. Their wallpaper group of (001)-projection is p4g composed of two perpendicular glide lines, which may give birth to wallpaper fermion and higher-order topology as discussed above.

The orbitally resolved band structures of Tl_4XTe_3 without and with SOC are illustrated in Fig. 2e–h. In the absence of SOC, Tl-p_z and Pb/Sn-p_z orbitals contribute to the conduction band minimum (CBM), while the valence band maximum (VBM) is dominated by Te-p_z orbitals with direct energy gaps of 142 meV and 16 meV for Tl_4PbTe_3 and Tl_4SnTe_3, respectively, as illustrated in Fig. 2e, f. Switching on SOC, the insulating character is preserved for both Tl_4PbTe_3 and Tl_4SnTe_3 with corresponding energy gaps of 83 meV and 20 meV, which are similar to previous predictions[60,61], and remarkably, an inversion of the orbital characters around the Γ point occurs as shown in Fig. 2g, h. However, qualitatively different from the reported *s-p* or *p-p* band inversions in TIs and TCIs, the parity of Bloch state forms the CBM and VBM at Γ are all positive, i.e., there is no parity exchange between occupied and unoccupied bands in the SOC-induced *p-p* band inversion for Tl_4XTe_3. Compared to the elementary band representations (EBR) of the No.140 space group as tabulated in Bilbao Crystallographic Server, the co-

irreps of all occupied bands can be expressed as a combination of EBR with all positive integers:

$$\bar{E}_2@4a + 9\bar{E}_1@4a + 3^1\bar{E}_{2g}^2\bar{E}_{2g}@4c + {}^1\bar{E}_{1g}^2\bar{E}_{1g}@4c$$
$$+ 3^1\bar{E}_{2u}^2\bar{E}_{2u}@4c, \tag{3}$$

exhibiting an unobstructed atom insulator character.

To ensure the parity judgement, we implement the direct calculations of topological $\mathbb{Z}_2$ invariants v_0; (v_1, v_2, v_3) according to the parity of each Kramers pair at eight $\mathbb{T}$-invariant momenta (Λ_α)[67]. The number of odd and even bands are listed in Fig. 2c, and therefore the parity products at eight Λ_α are given as (+, −, −, +, +, −, −, +), that results in $v_0 = 0$ and (v_1, v_2, v_3) = (0, 0, 0), revealing the trivial $\mathbb{Z}_2$ property. In addition, as reported for TCIs with wallpaper fermions, one can always use the Wilson loop eigenvalues along the glide symmetry preserved surface to define two generalized $\mathbb{Z}_4$ invariants, (χ_x, χ_y), which can be evaluated by the crossing of each glide sector and an arbitrary horizontal line[19]. As presented in Fig. 4c–e, trivial generalized $\mathbb{Z}_4$ indices with (χ_x, χ_y) = (0, 0) are obtained, revealing the different topology from previous wallpaper fermions that is one of major characters for our wallpaper fermions.

Actually, the calculated $\mathbb{Z}_2$ and $\mathbb{Z}_4$ invariants agree with the previous works that classified Tl_4XTe_3 into trivial insulators[59–62], here remarkably, we further detail their topology, and identify them as the first realistic electronic material realizations of TOTIs with exotic wallpaper fermions and corner states. To prove the nontrivial topology, similar to the concept of time-reversal polarization[68], we define a time-reversal polarized octupole polarization based on the Wilson loop and nested Wilson loop. Firstly, 1st order Wilson loop along x, y and z-direction are calculated with 72 occupied bulk bands as shown in Fig. 4c–e. We choose half of the 1st Wilson bands to do the 2nd order Wilson loop by specifying two generalized 'Fermi levels', indicated with red dashed lines. The spectrum of 2nd order Wilson bands are shown in Fig. 4f–h. Since the 2nd order Wilson bands are still gaped, we can implement the calculations of 3rd order Wilson loop under six occupied 2nd order Wilson bands. All the six 3rd order Wilson bands show us a nontrivial value of 0.5, leading to a vanishing octupole polarization. However, we define a topological invariant quantity by taking one eigenvalue of each 3rd order Wilson
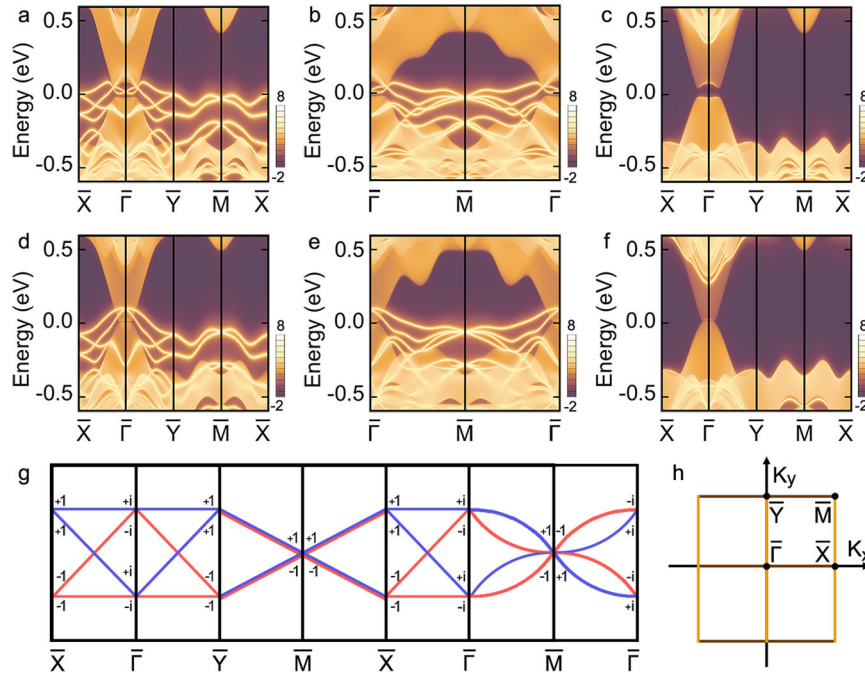
Fig. 3 Surface spectrum for wallpaper fermion. Band structures for (001) surface of **a–c** Tl_4PbTe_3 and **d–f** Tl_4SnTe_3 calculated using surface Green's functions. The Fermi level is set to zero. **a, b, d, e** The top surface displays hourglass fermions along the glide-symmetric lines $\overline{\Gamma X}/\overline{\Gamma Y}$ and the fourfold Dirac fermion at the $\overline{M}$ point, while **c, f** there is no surface bands on the bottom surface. **g** Schematic of wallpaper fermions along the glide-invariant lines $\mathbb{G}_{x/y}$. The labels indicate the corresponding eigenvalues $\pm ie^{-ik_{x/y}/2}$. **h** Brillouin zone of the (001)-surface with $\mathbb{G}_x/\mathbb{G}_y$ invariant lines are indicated by yellow/brown lines.

Kramers pair and making a summation, which should serve as the topological invariant for a nonmagnetic SOTI. The result shows us

$$\left(\tilde{p}_{x,+}^{+z,+y}, \tilde{p}_{y,+}^{+x,+z}, \tilde{p}_{z,+}^{+y,+x}\right) = \left(\frac{1}{2}, \frac{1}{2}, \frac{1}{2}\right), \tag{4}$$

demonstrating the TOTI nature of Tl_4XTe_3.

Nontrivial wallpaper fermions

The non-trivial $(d-1)$ dimensional topology of wallpaper fermions of Tl_4XTe_3 originate from two perpendicular glide planes $g_x = \{M_x|\frac{1}{2}\frac{1}{2}0\}$ and $g_y = \{M_y|\frac{1}{2}\frac{1}{2}0\}$. Those glide planes can only be on effects in their symmetry-preserving crystal surface, which need to perpendicular to the mirror planes and also invariant under the translation along the glide translation direction. The only surface that satisfies those conditions is the (001) surface with wallpaper group $p4g$. Figure 3a, b (3d and 3e) display the nontrivial surface states with hourglass fermion and fourfold-degenerate Dirac fermion for Tl_4PbTe_3 (Tl_4SnTe_3), and Fig. 3c (3f) presents the opposite (001) surface states. To understand the nature of these band crossings, we have to check the glide eigenvalues of the surface bands as shown in Fig. 3g. Along g_x (g_y) invariant line $\overline{\Gamma Y}$ ($\overline{\Gamma X}$), one of the Kramers pair at $\overline{\Gamma}$ changes its partner with one of the Kramer pairs at $\overline{Y}$ ($\overline{X}$), constituting so-called hourglass surface band structure. Along g_x (g_y) invariant line $\overline{MX}$ ($\overline{MY}$), bands are always doubly-degenerate instead of forming hourglass structure, which is caused by commutation relation of $g_x g_y = -g_y g_x t_x t_{-y}$, leading to only one kind of Irreps. The fourfold-degenerate Dirac point splits into quadruplets away from $\overline{M}$ along the $\overline{M\Gamma}$ because of either g_x or g_y is broken. The Möbius twist originates from the intrinsic translation part of glide planes. As we can see from the glide eigenvalues of $g_{\pm x} = \pm ie^{-ik_y/2}$ and $g_{\pm y} = \pm ie^{-ik_x/2}$, one band with eigenvalue $g_{+x/y}$ will turn into $g_{-x/y}$ instead of turning into itself like a mirror plane. Such unusual connectivity gives rise to the Möbius twist character, which is distinct from the symmorphic symmetry-protected TCIs.

Nontrivial helical corner states

At last, we investigate the emergence of nontrivial corner states in our systems, which are the hallmarks of 3D TOTIs, by using the maximally localized Wannier functions that can reproduce the band dispersions of Tl_4XTe_3 very accurately. Firstly, we construct a finite lattice composed of $6 \times 6 \times 6$ conventional unit cells as exemplified in Supplementary Figs. 1–3. Notably, as shown in Fig. 4a, b, 16 nearly degenerate states arise around the Fermi level, highlighted in red color. The results are further confirmed by using the more sophisticated Heyd–Scuseria–Ernzerhof hybrid functional method (HSE06)[69]. Larger energy gaps are obtained for both the Tl_4PbTe_3 and Tl_4SnTe_3, and remarkably, the corner states as well as the third-order topology remain intact (see Supplementary Fig. 4). The inset presents the corresponding real-space distribution of one corner state. Indeed, the wave functions of this state are localized almost at the 8 corners and vanish in other regions, which is a significant signal for the corner states. It is interesting to emphasize that 16 corner states are helical, different from the previous quantized octupole TIs with chiral modes[26,34,57,58]. Due to the degeneracy of 16 in-gap states, the half-filling condition cannot be satisfied as long as $\mathbb{P}$ is preserved, which is known as the filling anomaly. To resolve the filling anomaly, extra electrons or holes need to fulfill the valence band completely, which results in accumulations of electrons or holes.

DISCUSSION

In summary, We have proposed Tl_4XTe_3 (X = Pb/Te) as promising material candidates for both wallpaper fermions and TOTIs using k·p models and ab-initio calculations. Due to the existence of two perpendicular glide planes, the exotic hourglass fermion, four-fold degenerate Dirac fermion, and Möbius fermion can still emerge on the (001) surface. Different from the previous wallpaper fermions, our proposed materials have a trivial Z_4 invariant that is in agreement with the results of topological quantum chemistry.
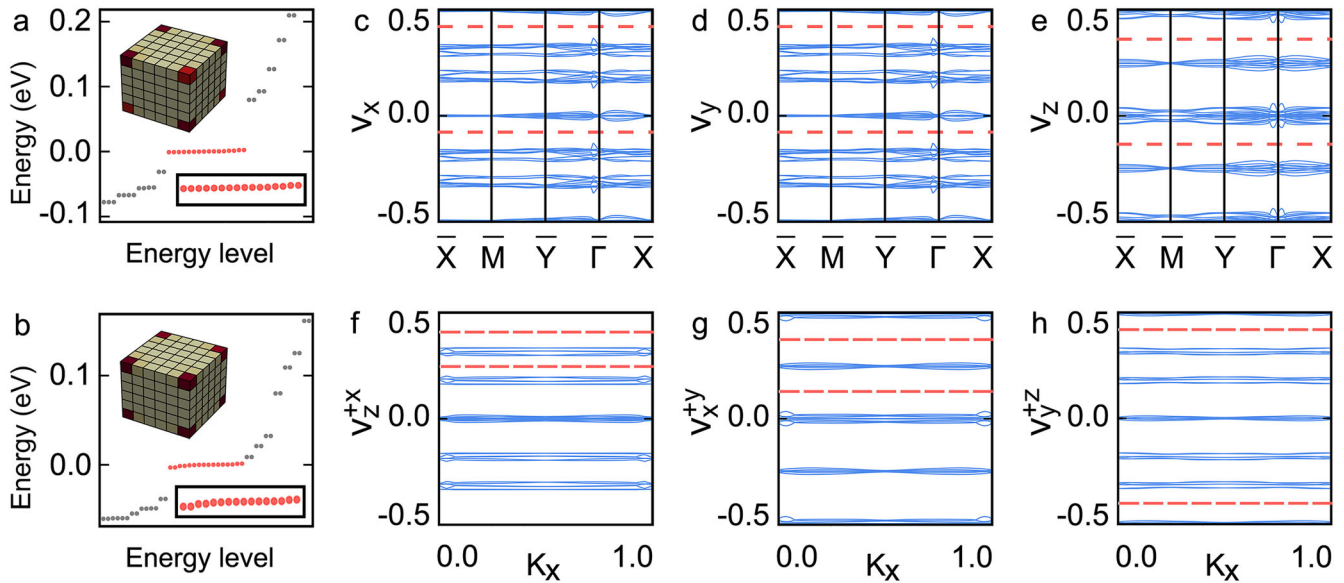
Fig. 4 Nontrivial helical corner states. Energy levels of a finite lattice composed of $6 \times 6 \times 6$ conventional unit cells for **a**, Tl_4PbTe_3 and **b**, Tl_4SnTe_3. There are 16 degenerate corner states as indicated with red color, which is magnified in the inset of **a, b**. Insets show the probability of one corner state, where we sum all contributions of probability in one unit cell and each unit cell is represented with a cubic. **c–e** 1st order Wilson bands v_x, v_y, and v_z of the occupied bulk bands. The generalized 'Fermi levels' are indicated with red dash lines, where we take the 1st order Wilson bands among the two red lines as occupied 1st order Wilson bands. **f–h** 2nd order Wilson bands v_z^{+x}, v_x^{+y}, and v_y^{+z} of the selected occupied 1st order Wilson bands. The generalized 'Fermi levels' are indicated with red dash lines, where we take the 2nd order Wilson bands among the two red lines as occupied 2nd order Wilson bands.

Especially, we generalize the third-order topology to nonsymmorphic symmetries, realizing the TOTI phase in the Tl_4XTe_3 system. Due to the existence of $\mathbb{T}$, corner states come in Kramers pair and have a zero octupole polarization, which is different from the quantized octupole TIs achieved in metamaterials[34,58]. Each one of the Kramers pair has a nontrivial octupole polarization, leading to a nontrivial time-reversal polarized octupole polarization. Our findings may motivate the formulation of strategies for finding topological phenomena and exotic topological states for spintronics applications.

METHODS
First-principles calculations
The first-principles calculations are carried out in the framework of generalized gradient approximation (GGA) with Perdew–Burke–Ernzerhof (PBE)[70] functionals using the Vienna Ab initio simulation package (VASP)[71] and the full-potential linearized augmented-plane-wave method using the FLEUR code[72]. The self-consistent total energy was evaluated with a $12 \times 12 \times 8$ k-point mesh, and the cutoff energy for the plane-wave basis set was 500 eV. The maximally localized Wannier functions (MLWFs) are constructed using the Wannier90 code[73] in conjunction with the FLEUR packag[74,75] and the surface states calculations are using WannierTools[76], where we choose p orbital of Pb/Sn, Te and Tl atoms and dismiss 64 lower-energy isolated bands to construct MLWFs. The Wilson loops are calculated by the wave function of MLWFs for the conventional unit cell. While $\mathbb{Z}_2$ and $\mathbb{Z}_4$ calculations are implemented with the wave function of WAVECAR file for the primitive unit cell. The symmetry elements of I4/mcm are adopted from International Tables of Crystallography[77].

DATA AVAILABILITY
The data that support the findings of this study are available from the corresponding author upon reasonable request.

CODE AVAILABILITY
The codes are available from the corresponding author upon reasonable request.

REFERENCES
1. Wang, C., Lin, C.-H. & Levin, M. Bulk-boundary correspondence for three-dimensional symmetry-protected topological phases. *Phys. Rev. X* **6**, 021015 (2016).
2. Chiu, C.-K., Teo, J. C. Y., Schnyder, A. P. & Ryu, S. Classification of topological quantum matter with symmetries. *Rev. Mod. Phys.* **88**, 035005 (2016).
3. Po, H. C., Vishwanath, A. & Watanabe, H. Symmetry-based indicators of band topology in the 230 space groups. *Nat. Commun.* **8**, 50 (2017).
4. Kruthoff, J., De Boer, J., Van Wezel, J., Kane, C. L. & Slager, R.-J. Topological classification of crystalline insulators through band structure combinatorics. *Phys. Rev. X* **7**, 041069 (2017).
5. Watanabe, H., Po, H. C. & Vishwanath, A. Structure and topology of band structures in the 1651 magnetic space groups. *Sci. Adv.* **4**, eaat8685 (2018).
6. Song, Z., Zhang, T., Fang, Z. & Fang, C. Quantitative mappings between symmetry and topology in solids. *Nat. Commun.* **9**, 3530 (2018).
7. Tang, F., Po, H. C., Vishwanath, A. & Wan, X. Topological materials discovery by large-order symmetry indicators. *Sci. Adv.* **5**, eaau8725 (2019).
8. Fu, L. Topological crystalline insulators. *Phys. Rev. Lett.* **106**, 106802 (2011).
9. Hsieh, T. H. et al. Topological crystalline insulators in the SnTe material class. *Nat. Commun.* **3**, 982 (2012).
10. Hsu, C.-H. et al. Purely rotational symmetry-protected topological crystalline insulator α-Bi$_4$Br$_4$. *2D Mater.* **6**, 031004 (2019).
11. Zhang, T. et al. Topological crystalline insulators with C_2 rotation anomaly. *Phys. Rev. Res.* **1**, 012001 (2019).
12. Wang, Z., Alexandradinata, A., Cava, R. J. & Bernevig, B. A. Hourglass fermions. *Nature* **532**, 189 (2016).
13. Ma, J. et al. Experimental evidence of hourglass fermion in the candidate nonsymmorphic topological insulator in KHgSb. *Sci. Adv.* **3**, e1602415 (2017).
14. Chang, P.-Y., Erten, O. & Coleman, P. Möbius kondo insulators. *Nat. Phys.* **13**, 794–798 (2017).
15. Zhang, R.-X., Wu, F. & Das Sarma, S. Möbius insulator and higher-order topology in MnBi$_{2n}$Te$_{3n+1}$. *Phys. Rev. Lett.* **124**, 136407 (2020).
16. Kane, C. L. & Mele, E. J. Quantum spin Hall effect in graphene. *Phys. Rev. Lett.* **95**, 226801 (2004).
17. Bernevig, B. A., Hughes, T. L. & Zhang, S.-C. Quantum spin Hall effect and topological phase transition in HgTe quantum wells. *Science* **314**, 1757–1761 (2006).

18. Zhang, H. et al. Topological insulators in Bi_2Se_3, Bi_2Te_3 and Sb_2Te_3 with a single Dirac cone on the surface. *Nat. Phys.* **5**, 438–442 (2009).

19. Wieder, B. J. et al. Wallpaper fermions and the nonsymmorphic Dirac insulator. *Science* **361**, 246–251 (2018).

20. Liu, C.-X., Zhang, R.-X. & VanLeeuwen, B. K. Topological nonsymmorphic crystalline insulators. *Phys. Rev. B* **90**, 085304 (2014).

21. Shiozaki, K., Sato, M. & Gomi, K. Z_2 topology in nonsymmorphic crystalline insulators: Möbius twist in surface states. *Phys. Rev. B* **91**, 155120 (2015).

22. Fang, C. & Fu, L. New classes of three-dimensional topological crystalline insulators: nonsymmorphic and magnetic. *Phys. Rev. B* **91**, 161105 (2015).

23. Yang, B.-J., Bojesen, T. A., Morimoto, T. & Furusaki, A. Topological semimetals protected by off-centered symmetries in nonsymmorphic crystals. *Phys. Rev. B* **95**, 075135 (2017).

24. Liu, Y. et al. Topological corner modes in a brick lattice with nonsymmorphic symmetry. *Phys. Rev. B* **102**, 035142 (2020).

25. Ryu, D.-C., Kim, J., Choi, H. & Min, B. I. Wallpaper Dirac fermion in a nonsymmorphic topological kondo insulator: PuB_4. *J. Am. Chem. Soc.* **142**, 19278–19282 (2020).

26. Benalcazar, W. A., Bernevig, B. A. & Hughes, T. L. Quantized electric multipole insulators. *Science* **357**, 61–66 (2017).

27. Benalcazar, W. A., Bernevig, B. A. & Hughes, T. L. Electric multipole moments, topological multipole moment pumping, and chiral hinge states in crystalline insulators. *Phys. Rev. B* **96**, 245115 (2017).

28. Schindler, F. et al. Higher-order topological insulators. *Sci. Adv.* **4**, eaat0346 (2018).

29. Xie, B. et al. Higher-order band topology. *Nat. Rev. Phys.* **3**, 520–532 (2021).

30. Liu, B., Zhao, G., Liu, Z. & Wang, Z. Two-dimensional quadrupole topological insulator in γ-graphyne. *Nano Lett.* **19**, 6492–6497 (2019).

31. Sheng, X.-L. et al. Two-dimensional second-order topological insulator in graphdiyne. *Phys. Rev. Lett.* **123**, 256402 (2019).

32. Zhang, X. et al. Symmetry-protected hierarchy of anomalous multipole topological band gaps in nonsymmorphic metacrystals. *Nat. Commun.* **11**, 1–9 (2020).

33. Lee, E., Kim, R., Ahn, J. & Yang, B.-J. Two-dimensional higher-order topology in monolayer graphdiyne. *npj Quantum Mater.* **5**, 1–7 (2020).

34. Ni, X., Li, M., Weiner, M., Alù, A. & Khanikaev, A. B. Demonstration of a quantized acoustic octupole topological insulator. *Nat. Commun.* **11**, 1–7 (2020).

35. Lin, Z.-K., Wang, H.-X., Xiong, Z., Lu, M.-H. & Jiang, J.-H. Anomalous quadrupole topological insulators in two-dimensional nonsymmorphic sonic crystals. *Phys. Rev. B* **102**, 035105 (2020).

36. Serra-Garcia, M. et al. Observation of a phononic quadrupole topological insulator. *Nature* **555**, 342–345 (2018).

37. Peterson, C. W., Benalcazar, W. A., Hughes, T. L. & Bahl, G. A quantized microwave quadrupole insulator with topologically protected corner states. *Nature* **555**, 346–350 (2018).

38. Schindler, F. et al. Higher-order topology in bismuth. *Nat. Phys.* **14**, 918–924 (2018).

39. Imhof, S. et al. Topolectrical-circuit realization of topological corner modes. *Nat. Phys.* **14**, 925–929 (2018).

40. Yue, C. et al. Symmetry-enforced chiral hinge states and surface quantum anomalous Hall effect in the magnetic axion insulator $Bi_{2-x}Sm_xSe_3$. *Nat. Phys.* **15**, 577–581 (2019).

41. Zhang, X. et al. Second-order topology and multidimensional topological transitions in sonic crystals. *Nat. Phys.* **15**, 582–588 (2019).

42. Zhang, D. et al. Topological axion states in the magnetic insulator $MnBi_2Te_4$ with the quantized magnetoelectric effect. *Phys. Rev. Lett.* **122**, 206401 (2019).

43. Xu, Y., Song, Z., Wang, Z., Weng, H. & Dai, X. Higher-order topology of the axion insulator $EuIn_2As_2$. *Phys. Rev. Lett.* **122**, 256402 (2019).

44. Kempkes, S. et al. Robust zero-energy modes in an electronic higher-order topological insulator. *Nat. Mater.* **18**, 1292–1297 (2019).

45. Park, M. J., Kim, Y., Cho, G. Y. & Lee, S. Higher-order topological insulator in twisted bilayer graphene. *Phys. Rev. Lett.* **123**, 216803 (2019).

46. Zhang, X. et al. Dimensional hierarchy of higher-order topology in three-dimensional sonic crystals. *Nat. Commun.* **10**, 1–10 (2019).

47. Xue, H., Yang, Y., Gao, F., Chong, Y. & Zhang, B. Acoustic higher-order topological insulator on a kagome lattice. *Nat. Mater.* **18**, 108–112 (2019).

48. Ni, X., Weiner, M., Alu, A. & Khanikaev, A. B. Observation of higher-order topological acoustic states protected by generalized chiral symmetry. *Nat. Mater.* **18**, 113–120 (2019).

49. Liu, C. et al. Robust axion insulator and chern insulator phases in a two-dimensional antiferromagnetic topological insulator. *Nat. Mater.* **19**, 522–527 (2020).

50. Chen, C. et al. Universal approach to magnetic second-order topological insulator. *Phys. Rev. Lett.* **125**, 056402 (2020).

51. Xu, Y. et al. High-throughput calculations of magnetic topological materials. *Nature* **586**, 702–707 (2020).

52. Noguchi, R. et al. Evidence for a higher-order topological insulator in a three-dimensional material built from van der waals stacking of bismuth-halide chains. *Nat. Mater.* **20**, 473–479 (2021).

53. Song, Z., Fang, Z. & Fang, C. (d - 2)-dimensional edge states of rotation symmetry protected topological states. *Phys. Rev. Lett.* **119**, 246402 (2017).

54. Benalcazar, W. A., Li, T. & Hughes, T. L. Quantization of fractional corner charge in C_n-symmetric higher-order topological crystalline insulators. *Phys. Rev. B* **99**, 245151 (2019).

55. Nag, T., Juričić, V. & Roy, B. Hierarchy of higher-order floquet topological phases in three dimensions. *Phys. Rev. B* **103**, 115308 (2021).

56. Peterson, C. W., Li, T., Benalcazar, W. A., Hughes, T. L. & Bahl, G. A fractional corner anomaly reveals higher-order topology. *Science* **368**, 1114–1118 (2020).

57. Xue, H. et al. Realization of an acoustic third-order topological insulator. *Phys. Rev. Lett.* **122**, 244301 (2019).

58. Liu, S. et al. Octupole corner state in a three-dimensional topological circuit. *Light Sci. Appl.* **9**, 1–9 (2020).

59. Arpino, K. et al. Evidence for topologically protected surface states and a superconducting phase in $[Tl_4](Tl_{1-x}Sn_x)Te_3$ using photoemission, specific heat, and magnetization measurements, and density functional theory. *Phys. Rev. Lett.* **112**, 017002 (2014).

60. Vergniory, M. et al. A complete catalogue of high-quality topological materials. *Nature* **566**, 480–485 (2019).

61. Zhang, T. et al. Catalogue of topological electronic materials. *Nature* **566**, 475–479 (2019).

62. Tang, F., Po, H. C., Vishwanath, A. & Wan, X. Comprehensive search for topological materials using symmetry indicators. *Nature* **566**, 486–489 (2019).

63. Kosuga, A., Kurosaki, K., Muta, H. & Yamanaka, S. Thermoelectric properties of tl–x–te (x= ge, sn, and pb) compounds with low lattice thermal conductivity. *J. Appl. Phys.* **99**, 063705 (2006).

64. Barchij, I. et al. Tl_4SnS_3, Tl_4SnSe_3 and Tl_4SnTe_3 crystals as novel IR induced optoelectronic materials. *J. Mater. Sci. Mater. Electron* **27**, 3901–3905 (2016).

65. Filep, M., Sabov, M. Y., Barchiy, I., Plucinski, K. & Solomon, A. Interactions in the ternary reciprocal system Tl_2S + $SnTe$ ↔Tl_2Te+ SnS. *Chem. Met. Alloy.* **6**, 125–129 (2013).

66. Aroyo, M. I. et al. Bilbao crystallographic server: I. databases and crystallographic computing programs. *Z. Kristallogr. Cryst. Mater.* **221**, 15–27 (2006).

67. Fu, L. & Kane, C. L. Topological insulators with inversion symmetry. *Phys. Rev. B* **76**, 045302 (2007).

68. Fu, L. & Kane, C. L. Time reversal polarization and a Z_2 adiabatic spin pump. *Phys. Rev. B* **74**, 195312 (2006).

69. Krukau, A. V., Vydrov, O. A., Izmaylov, A. F. & Scuseria, G. E. Influence of the exchange screening parameter on the performance of screened hybrid functionals. *J. Chem. Phys.* **125**, 224106 (2006).

70. Perdew, J. P., Burke, K. & Ernzerhof, M. Generalized gradient approximation made simple. *Phys. Rev. Lett.* **77**, 3865 (1996).

71. Kresse, G. & Furthmüller, J. Efficient iterative schemes for ab initio total-energy calculations using a plane-wave basis set. *Phys. Rev. B* **54**, 11169–11186 (1996).

72. See http://www.flapw.de.

73. Pizzi, G. et al. Wannier90 as a community code: new features and applications. *J. Phys. Condens. Matter* **32**, 165902 (2020).

74. Mostofi, A. A. et al. Wannier90: a tool for obtaining maximally-localised wannier functions. *Comput. Phys. Commun.* **178**, 685–699 (2008).

75. Freimuth, F., Mokrousov, Y., Wortmann, D., Heinze, S. & Blügel, S. Maximally localized Wannier functions within the FLAPW formalism. *Phys. Rev. B* **78**, 035120 (2008).

76. Wu, Q., Zhang, S., Song, H.-F., Troyer, M. & Soluyanov, A. A. Wanniertools: an open-source software package for novel topological materials. *Comput. Phys. Commun.* **224**, 405–416 (2018).

77. Aroyo, M. I. International Tables for Crystallography. 6th Edition, Vol. **A** (Springer, 2016).

ACKNOWLEDGEMENTS

AUTHOR CONTRIBUTIONS

C.N. and Y.D. conceived the project. N.M. performed the first-principles calculations and model analysis with the help of H.W. and C.N. N.M. and C.N. wrote the manuscript with contributions from B.H. and Y.D. All authors discussed the results and commented on the manuscript.

COMPETING INTERESTS

The authors declare no competing interests.

ADDITIONAL INFORMATION

Supplementary information The online version contains supplementary material available at https://doi.org/10.1038/s41524-022-00839-y.

Correspondence and requests for materials should be addressed to Ying Dai or Chengwang Niu.

Reprints and permission information is available at http://www.nature.com/reprints